direction. Three different pipette solutions were used: Cs-gluconate solution (150 mM CsOH, 5 mM CsCl, 135 mM sucrose, 10 mM HEPES, 1.5 mM EGTA and 1.5 mM EDTA (pH 7.2 with D-gluconic acid)); Na-gluconate solution (150 mM Na-gluconate, 5 mM NaCl, 135 mM sucrose, 10 mM HEPES, 1.5 mM EGTA and 1.5 mM EDTA (pH 7.2 with NaOH)); Na-gluconate solution without Ca^{2+} buffer (150 mM Na-gluconate, 5 mM NaCl, 135 mM sucrose, 10 mM HEPES (pH 7.2 with NaOH)).

Signals were recorded using an Axopatch 200B patch-clamp amplifier, filtered at 5 kHz, and sampled at 10 kHz. Capacitance of the whole-mitoplast membrane ranged from 0.35 to 1 pF. Access resistances, usually 30–60 MΩ, were compensated by about 70%. Bath Ca^{2+} concentration was varied from 20 μM to 5 mM by addition of the corresponding amount of 1 M $CaCl_2$ stock solution into one of two solutions: Na-gluconate solution (150 mM Na-gluconate, 10 mM HEPES (pH 7.2 with NaOH)) or HEPES-Tris solution (205 mM HEPES (pH 7.2 with Trisma base)). Bath solution with 105 mM $[Ca^{2+}]_c$ (105 mM $CaCl_2$ solution) contained 105 mM $CaCl_2$, 10 mM HEPES (pH 7.2 with Trisma base or NaOH). This solution was dissolved with Na-gluconate solution or HEPES-Tris solution to obtain 26 mM $[Ca^{2+}]_c$. Bath solutions with 5 mM of Sr^{2+}, Ba^{2+}, Mn^{2+} or Mg^{2+} were obtained by addition of 1 M stock solution of the chloride salt into HEPES-Tris solution. HEPES-K bath solution (KOH 75 mM (pH 7.2 with about 210 mM HEPES)); HEPES-Na bath solution (NaOH 75 mM (pH 7.2 with about 210 mM HEPES)); Na-gluconate and K-gluconate low-divalent solutions (150 mM Na(K)-gluconate, 10 mM HEPES, 5 mM EGTA, 5 mM EDTA (pH 7.2 with NaOH)). $CaCl_2$ or $MgCl_2$ was added to Na-gluconate low-divalent (divalent-free) solution in the amounts calculated by the WinMAXC v2.05 program (C. Patton, Stanford University) to obtain free Ca^{2+} and Mg^{2+} concentrations. Osmolarity was approximately 280 mmol kg^{-1}. Statistical data was calculated as the mean ± s.d.

Single-channel recordings

All single-channel recordings were made in the inside-out configuration of the patch-clamp technique. Patches were excised from the inner mitochondrial membrane in a bath solution containing 150 mM Na-gluconate, 10 mM HEPES, 1 mM EGTA and 1 mM EDTA (pH 7.2 with NaOH). Pipettes were filled with 105 mM $CaCl_2$ solution. A total of 105 mM $CaCl_2$ solution was also used as the bath solution for single channels and whole-mitoplast recordings. Signals were filtered at 1 kHz and sampled at 5 kHz. In Supplementary Fig. 2, traces were filtered at 200 Hz before amplitude analysis.

Estimation of Ca^{2+}- and Mg^{2+}-binding constants

Ca^{2+} buffering is unreliable below 10 nM. To estimate the MiNa Ca^{2+}-binding constant, we assumed that I_{MiNa} in low-divalent solution was $\leq I_{MiNa}$ at theoretical 0 $[Ca^{2+}]_c$. Given that I_{MiNa} at 10 nM $[Ca^{2+}]_c$ was about eightfold less than I_{MiNa} in low-divalent solution, the Ca^{2+}-binding equilibrium constant calculated from the Hill equation was ≤2 nM assuming a Hill coefficient of 1. Similarly, the MiNa-binding constant for Mg^{2+} was estimated to be ≤250 nM.

Received 20 August; accepted 18 November 2003; doi:10.1038/nature02246.

1. Rizzuto, R., Bernardi, P. & Pozzan, T. Mitochondria as all-round players of the calcium game. *J. Physiol. (Lond.)* **529,** 37–47 (2000).
2. Montero, M. *et al.* Chromaffin-cell stimulation triggers fast millimolar mitochondrial Ca^{2+} transients that modulate secretion. *Nature Cell Biol.* **2,** 57–61 (2000).
3. McCormack, J. G., Halestrap, A. P. & Denton, R. M. Role of calcium ions in regulation of mammalian intramitochondrial metabolism. *Physiol. Rev.* **70,** 391–425 (1990).
4. Hajnoczky, G., Robb-Gaspers, L. D., Seitz, M. B. & Thomas, A. P. Decoding of cytosolic calcium oscillations in the mitochondria. *Cell* **82,** 415–424 (1995).
5. Jouaville, L. S., Ichas, F., Holmuhamedov, E. L., Camacho, P. & Lechleiter, J. D. Synchronization of calcium waves by mitochondrial substrates in *Xenopus laevis* oocytes. *Nature* **377,** 438–441 (1995).
6. Budd, S. L. & Nicholls, D. G. A re-evaluation of the role of mitochondria in neuronal Ca^{2+} homeostasis. *J. Neurochem.* **66,** 403–411 (1996).
7. Babcock, D. F., Herrington, J., Goodwin, P. C., Park, Y. B. & Hille, B. Mitochondrial participation in the intracellular Ca^{2+} network. *J. Cell Biol.* **136,** 833–844 (1997).
8. Boitier, E., Rea, R. & Duchen, M. R. Mitochondria exert a negative feedback on the propagation of intracellular Ca^{2+} waves in rat cortical astrocytes. *J. Cell Biol.* **145,** 795–808 (1999).
9. Scorrano, L. *et al.* BAX and BAK regulation of endoplasmic reticulum Ca^{2+}: a control point for apoptosis. *Science* **300,** 135–139 (2003).
10. Demaurex, N. & Distelhorst, C. Cell biology. Apoptosis—the calcium connection. *Science* **300,** 65–67 (2003).
11. Gunter, K. K. & Gunter, T. E. Transport of calcium by mitochondria. *J. Bioenerg. Biomembr.* **26,** 471–485 (1994).
12. Bernardi, P. Mitochondrial transport of cations: channels, exchangers, and permeability transition. *Physiol. Rev.* **79,** 1127–1155 (1999).
13. Gunter, T. E. & Pfeiffer, D. R. Mechanisms by which mitochondria transport calcium. *Am. J. Physiol.* **258,** C755–C786 (1990).
14. DeLuca, H. F. & Engstrom, G. W. Calcium uptake by rat kidney mitochondria. *Proc. Natl Acad. Sci. USA* **47,** 1744–1750 (1961).
15. Rizzuto, R., Brini, M., Murgia, M. & Pozzan, T. Microdomains with high Ca^{2+} close to IP_3-sensitive channels that are sensed by neighboring mitochondria. *Science* **262,** 744–747 (1993).
16. Neher, E. Vesicle pools and Ca^{2+} microdomains: new tools for understanding their roles in neurotransmitter release. *Neuron* **20,** 389–399 (1998).
17. Tashmukhamedov, B. A., Gagelgans, A. I., Mamatkulov, K. & Makhmudova, E. M. Inhibition of Ca^{2+} transport in mitochondria by selective blockade of membrane mucopolysaccharides by hexamine cobalt chloride. *FEBS Lett.* **28,** 239–242 (1972).
18. Ying, W. L., Emerson, J., Clarke, M. J. & Sanadi, D. R. Inhibition of mitochondrial calcium ion transport by an oxo-bridged dinuclear ruthenium amine complex. *Biochemistry* **30,** 4949–4952 (1991).
19. Matlib, M. A. *et al.* Oxygen-bridged dinuclear ruthenium amine complex specifically inhibits Ca^{2+} uptake into mitochondria *in vitro* and *in situ* in single cardiac myocytes. *J. Biol. Chem.* **273,** 10223–10231 (1998).
20. Drahota, Z., Gazzotti, P., Carafoli, E. & Rossi, C. S. A comparison of the effects of different divalent cations on a number of mitochondrial reactions linked to ion translocation. *Arch. Biochem. Biophys.* **130,** 267–273 (1969).
21. Vainio, H., Mela, L. & Chance, B. Energy dependent bivalent cation translocation in rat liver mitochondria. *Eur. J. Biochem.* **12,** 387–391 (1970).
22. Selwyn, M. J., Dawson, A. P. & Dunnett, S. J. Calcium transport in mitochondria. *FEBS Lett.* **10,** 1–5 (1970).
23. Kostyuk, P. G. & Krishtal, O. A. Effects of calcium and calcium-chelating agents on the inward and outward current in the membrane of mollusc neurones. *J. Physiol. (Lond.)* **270,** 569–580 (1977).
24. Almers, W., McCleskey, E. W. & Palade, P. T. A non-selective cation conductance in frog muscle membrane blocked by micromolar external calcium ions. *J. Physiol. (Lond.)* **353,** 565–583 (1984).
25. McCleskey, E. W. & Almers, W. The Ca channel in skeletal muscle is a large pore. *Proc. Natl Acad. Sci. USA* **82,** 7149–7153 (1985).
26. Prakriya, M. & Lewis, R. S. CRAC channels: activation, permeation, and the search for a molecular identity. *Cell Calcium* **33,** 311–321 (2003).
27. Vinogradov, A. & Scarpa, A. The initial velocities of calcium uptake by rat liver mitochondria. *J. Biol. Chem.* **248,** 5527–5531 (1973).
28. Bragadin, M., Pozzan, T. & Azzone, G. F. Kinetics of Ca^{2+} carrier in rat liver mitochondria. *Biochemistry* **18,** 5972–5978 (1979).
29. Hille, B. *Ion Channels of Excitable Membranes* (Sinauer Associates, Sunderland, Massachusetts, 2001).
30. Cannon, B. & Lindberg, O. Mitochondria from brown adipose tissue: isolation and properties. *Methods Enzymol.* **55,** 65–78 (1979).

Supplementary Information accompanies the paper on **www.nature.com/nature**.

Acknowledgements We would like to thank J. Borecky for advice on the whole-mitoplast configuration; L. DeFelice, H. Xu, B. Desai, V. Sandler and P. Smith for discussions; and S. Gapon and Y. Manasian for technical assistance.

Competing interests statement The authors declare that they have no competing financial interests.

Correspondence and requests for materials should be addressed to D.E.C. (dclapham@enders.tch.harvard.edu).

Two mitotic kinesins cooperate to drive sister chromatid separation during anaphase

Gregory C. Rogers[1], Stephen L. Rogers[2], Tamara A. Schwimmer[1], Stephanie C. Ems-McClung[3], Claire E. Walczak[3], Ronald D. Vale[2], Jonathan M. Scholey[4] & David J. Sharp[1]

[1]*Department of Physiology and Biophysics, Albert Einstein College of Medicine, Bronx, New York 10461, USA*
[2]*The Howard Hughes Medical Institute and Department of Cellular and Molecular Pharmacology, University of California, San Francisco, California 94143, USA*
[3]*Medical Sciences Program, Indiana University, Bloomington, Indiana 47405, USA*
[4]*Center for Genetics and Development and Section of Molecular and Cellular Biology, University of California, Davis, California 95616, USA*

During anaphase identical sister chromatids separate and move towards opposite poles of the mitotic spindle[1,2]. In the spindle, kinetochore microtubules[3] have their plus ends embedded in the kinetochore and their minus ends at the spindle pole. Two models have been proposed to account for the movement of chromatids during anaphase. In the 'Pac-Man' model, kinetochores induce the depolymerization of kinetochore microtubules at their plus ends, which allows chromatids to move towards the pole by 'chewing up' microtubule tracks[4,5]. In the 'poleward flux' model, kinetochores anchor kinetochore microtubules and chromatids are pulled towards the poles through the depolymerization of kinetochore microtubules at the minus ends[6]. Here, we show that two functionally distinct microtubule-destabilizing KinI kinesin

enzymes (so named because they possess a kinesin-like ATPase domain positioned internally within the polypeptide) are responsible for normal chromatid-to-pole motion in *Drosophila*. One of them, KLP59C, is required to depolymerize kinetochore microtubules at their kinetochore-associated plus ends, thereby contributing to chromatid motility through a Pac-Man-based mechanism. The other, KLP10A, is required to depolymerize microtubules at their pole-associated minus ends, thereby moving chromatids by means of poleward flux.

Although molecules involved in either Pac-Man- or poleward-flux-based motility mechanisms (see Supplementary Fig. S1) have not been identified previously, members of the KinI subfamily of kinesins are logical candidates for both[7]. These proteins bind directly to the ends of microtubules and promote their disassembly *in vitro*[8–10]. Moreover, the inhibition of KinI proteins in mitotic cells from various systems has been shown to disrupt mitosis[11–13]. To identify novel KinI family members in *Drosophila melanogaster*, we searched *Drosophila* genome databases for genes that share significant identity with the known KinI catalytic domains from other species. This revealed three different *D. melanogaster* genes predicted to encode products containing internal kinesin domains highly similar to vertebrate KinI (65% amino acid identity on average; Supplementary Fig. S2). We refer to these as KLP10A, KLP59C and KLP59D (kinesin-like protein at cytological regions 10A, 59C and 59D; ref. 14). Notably, we observed that purified recombinant polypeptides corresponding to the catalytic domains of KLP10A and KLP59C destabilize microtubules in an ATP-dependent fashion (Supplementary Fig. S3). (Similar analysis of KLP59D has not yet been performed but the high degree of amino acid identity among the catalytic domains of all three *Drosophila* KinI proteins (66% on average) suggests that it will also possess microtubule-destabilizing activity.) Thus, *Drosophila* probably possesses three distinct microtubule-destabilizing KinI kinesins.

Analysis of *Drosophila* S2 tissue culture cells depleted of each of the three KinI proteins (individually and in various combinations) using double-stranded RNA interference (RNAi) suggests that both KLP10A and KLP59C perform important but distinct mitotic functions (Supplementary Figs S4g, S5 and Table S1). KLP10A depletion by RNAi treatment causes a marked perturbation of mitotic spindle architecture (Fig. 1b–e). In contrast, KLP59C RNAi treatment has no noticeable impact on mitotic spindle structure but does significantly elevate the frequency with which chromosome segregation defects are observed (Fig. 1g–i). Immunolocalization of these proteins in mitotic S2 cells also reveals distinctions that may provide insights into their specific mitotic mechanisms of action. Specifically, KLP10A, similarly to vertebrate KinI proteins, localizes to mitotic centrosomes, spindle poles and centromeres through metaphase (Fig. 1j; see also Supplementary Fig. S6). However, the centromeric localization of KLP10A diminishes markedly at the onset of anaphase, leaving the majority of KLP10A immunostaining on the spindle poles (Fig. 1k). KLP59C, on the other hand, appears to be primarily restricted to centromeric regions of chromosomes during both metaphase and anaphase, and no KLP59C immunostaining is detectable on spindle poles throughout mitosis (Fig. 1l, m; see also Supplementary Fig. S6).

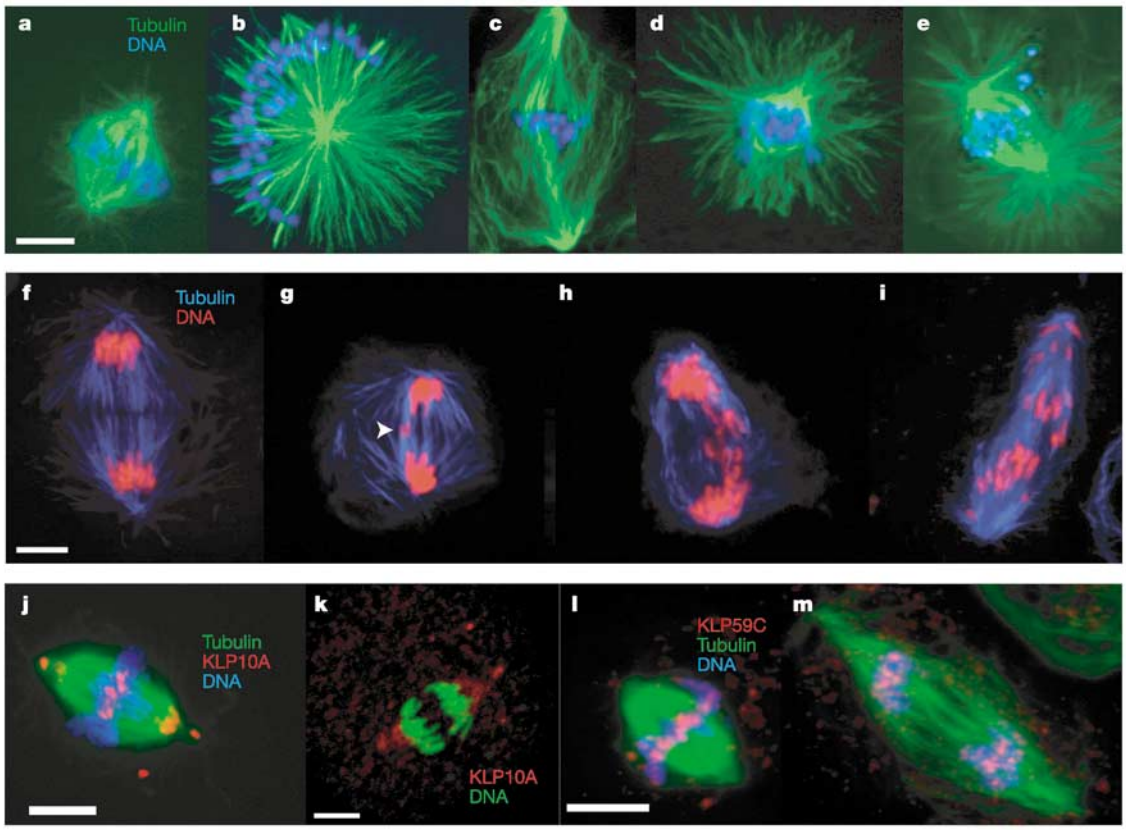

Figure 1 KLP10A and KLP59C perform distinct functions and localize to distinct sites in mitotic cells. **a**–**e**, Mitotic spindles from control (**a**) and KLP10A RNAi-treated (**b**–**e**) S2 cultures. Defects observed after KLP10A RNAi treatment consistently fall into one of four classes: monopolar spindles (**b**); long metaphase figures with disorganized central spindles (**c**); microtubule baskets forming around chromosomes (**d**); spindles with abnormally long astral microtubules (**e**). **f**–**i**, Anaphase spindles displaying normal (**f**) and defective (**g**–**i**) chromosome segregation. KLP59C RNAi treatment elevates the frequency of defective chromosome segregation (KLP59C RNAi, 42.9 ± 1%; control, 23 ± 1%; $P < 0.0002$). **j**–**m**, Localization of KLP10A (**j**, **k**) and KLP59C (**l**, **m**) during metaphase (**j**, **l**) and anaphase (**k**, **m**). Scale bar, 5 mm.

Thus, during chromatid-to-pole motion in anaphase, KLP10A and KLP59C are positioned appropriately to interact with the opposite ends of kinetochore microtubules: KLP10A concentrates around the minus ends of kinetochore microtubules focused at the poles, whereas KLP59C is positioned to act on the plus ends of kinetochore microtubules embedded in the kinetochore. Finally, our analyses of KLP59D do not support a role for this protein in spindle assembly or chromosome segregation, and its cellular functions will be reported elsewhere.

The specific mechanisms of action of mitotic KLP10A and KLP59C are impossible to discern from fixed samples. Therefore, we used living *Drosophila* syncytial blastoderm-stage embryos to elucidate the dynamic events leading to the mitotic phenotypes described in KLP10A- and KLP59C-deficient S2 cultures. These embryos are ideal for such analyses because they contain a monolayer of adjacent nuclei, within the same cytoplasm, that proceed through mitosis synchronously and relatively rapidly[15]. Moreover, these cells lack a standard mitotic spindle checkpoint, which normally delays cells in prometaphase in response to spindle damage, allowing mitotic proteins that might function later in the cell cycle to be assessed[16]. For our studies, soluble KinI inhibitors (Supplementary Figs S2c, S4a–f and S8a) and fluorescent tubulin or histones were microinjected into living transgenic embryos expressing different green fluorescent protein (GFP)-tagged spindle proteins. This allows the dynamic behaviour of spindle components to be visualized in the presence and absence of specific KinI inhibitors. (Supplementary Movies 1 and 2 show mitosis in control-injected embryos).

The introduction of KLP10A inhibitors into embryos rapidly alters the organization of mitotic spindle microtubules, as revealed by time-lapse imaging of anti-KLP10A antibody-injected transgenic embryos expressing GFP–tubulin as a microtubule marker (Fig. 2). Within 2 min of antibody injection, the concentration of microtubules at centrosomes increases significantly compared with controls. The relative fluorescent intensities of GFP–tubulin in both prophase and metaphase domains were on average 1.4-fold higher in regions proximal to the injection site compared with mitotic domains at more distal sites (Supplementary Table S2). Thus, KLP10A normally limits the growth/density of microtubules at centrosomes. Subsequently, severe defects in mitotic spindle assembly become apparent (Fig. 2a; see also Supplementary Movie 3). These can be categorized into two classes (Supplementary Table S3). Thirty per cent formed monopolar spindles, which assemble when centrosomes (partially separated during prophase) collapse back together at a rate of $0.019\,\mu m\,s^{-1}$ after nuclear envelope breakdown (class one). These structures may result from general defects in the organization of centrosomal microtubules. A total of 61% display abnormally long bipolar spindles, which often form adjacent to monopolar spindles (class two). These bipolar spindles elongate continuously during prometaphase through anaphase and attain metaphase lengths approximately twice that of controls (Fig. 2c). Notably, the rate of elongation of these spindles

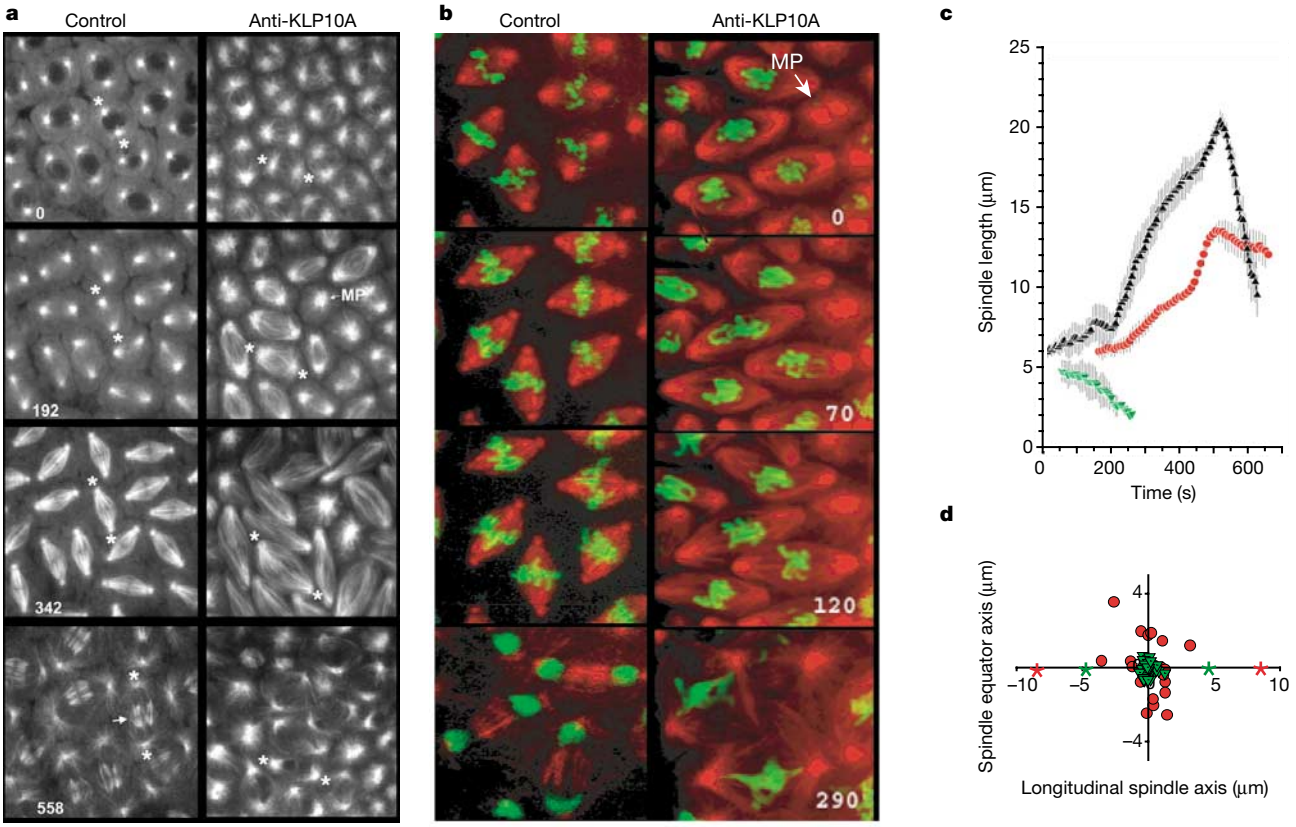

Figure 2 KLP10A inhibition perturbs mitotic spindle assembly and chromosome segregation. **a**, **b**, Time series of images showing mitosis in control (left) and anti-KLP10A-injected (right) embryos. Embryos in **a** express GFP–tubulin, allowing spindles to be visualized, whereas those in **b** contain rhodamine–tubulin and GFP–histones, allowing simultaneous visualization of spindles (red) and chromosomes (green). Time (in seconds), centrosomes from selected spindles (asterisk), monopolar spindles (MP), and telophase midbody (arrow) are marked. **c**, Plots comparing spindle length over time in control and anti-KLP10A-injected embryos. Plots begin at prometaphase. Red circles, control injected; green triangles, monopolar spindles from anti-KLP10A-injected embryos; black triangles, bipolar spindles from anti-KLP10A-injected embryos. **d**, Graph of the average centroid positions of GFP–Cid-labelled kinetochores on spindles in control (green triangles) and anti-KLP10A-injected (red circles) embryos. Red stars mark the average position of spindle poles in spindles from KLP10A-inhibited embryos and green stars mark the average position of poles from controls.

before anaphase is nearly identical to the rate of anaphase B spindle elongation in controls (peak rate (±s.d.) for anti-KLP10A is $0.061 \pm 0.006\,\mu m\,s^{-1}$, $n = 10$, and for controls is $0.062 \pm 0.008\,\mu m\,s^{-1}$, $n = 10$). The implications of this observation are discussed below. Finally, during telophase, midbodies fail to form on these spindles and centrosomes 'snap-back' together.

In addition to spindle defects, KLP10A inhibition in embryos perturbs the movement and segregation of chromosomes (Fig. 2b; see also Supplementary Movie 4). Specifically, the motility of individual chromosomes during prometaphase is often incoherent in treated embryos and subsequently, during metaphase, the majority of chromosomes and kinetochores fail to align properly at the metaphase plate. Instead, they are scattered around the spindle equator (Fig. 2d). Finally, during anaphase, chromatids translocate towards spindle poles at rates significantly slower than controls (average rate: $0.054\,\mu m\,s^{-1}$ anti-KLP10A; $0.094\,\mu m\,s^{-1}$ controls; Supplementary Table S4). This results in a significant increase in severe chromosome segregation defects such as stretched or bi-lobed chromosome masses (Supplementary Fig. S7 and Table S3). These anaphase phenotypes are observed regardless of whether kinetochores congressed properly to the metaphase plate or not. Indistinguishable results were obtained using monovalent Fab fragments (Supplementary Fig. S8b) and were corroborated using a recombinant dominant/negative construct (Supplementary Fig. S9).

In contrast to our findings for KLP10A, the introduction of KLP59C inhibitors into embryos has no apparent effect on the organization of mitotic spindles (Fig. 3a, c; see also Supplementary Movie 5 and Table S3). However, KLP59C inhibition does produce significant defects in chromosome positioning and motility (Supplementary Fig. S7 and Table S3). Chromosomes and kinetochores fail to align tightly at the spindle equator during metaphase under these conditions (Fig. 3d). Moreover, KLP59C inhibition prevents normal chromosome segregation during anaphase (Fig. 3b). Failures in chromosome segregation do not seem to result from decondensation of lagging chromosomes at the metaphase plate, nor are they due to non-disjunction of sister chromatids, because kinetochores do segregate to opposite sides of the chromosomal mass (Fig. 3b). Instead, as with KLP10A, the rate of chromatid-to-pole motion is slowed significantly in KLP59C-inhibited embryos (average rate: $0.042\,\mu m\,s^{-1}$ anti-KLP59C; $0.094\,\mu m\,s^{-1}$ controls; Supplementary Table S4). (These effects were reproduced by Fabs and a dominant/negative construct (Supplementary Fig. S8a, c and S9).)

Given the possibility of nonspecific effects, we investigated the mechanism of protein perturbation induced by antibody injections. The antibodies used in our experiments were raised against recombinant amino-terminal targeting domains (NT) of the *Drosophila* KinI kinesins[11] (Supplementary Fig. S2c). Thus, we reasoned that injection of these antibodies would specifically inhibit KinI function by displacing endogenous KLP10A and KLP59C from spindles[13]. Fluorescently labelled NT polypeptides mimic the spindle localization of endogenous KLP10A and KLP59C when injected into embryos: the 10A-NT protein localizes to centrosomes, spindle poles and metaphase centromeres, whereas 59C-NT localizes to centromeres (Supplementary Fig. S10). Therefore, these fluorescent constructs could be used to report the behaviour of the endogenous proteins *in vivo*. Consistent with the hypothesis that our KinI antibodies displace endogenous KinI proteins, the 10A-NT and 59C-NT proteins were rapidly mis-localized from spindle and/or chromosomal sites after the injection of anti-KLP10A and anti-KLP59C antibodies, respectively. In contrast, the reciprocal experiments do not produce this effect (for example, anti-KLP59C antibodies do not mis-localize the 10A-NT construct and vice versa). Moreover, injected fluorescently labelled antibodies often form cytoplasmic aggregates that co-localize with aggregates of the

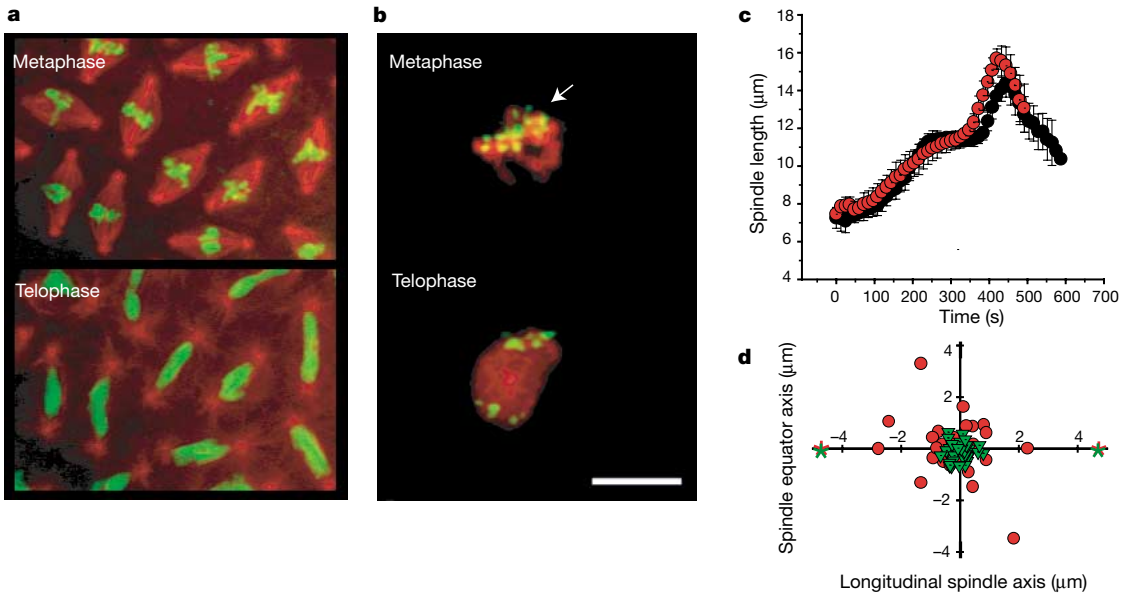

Figure 3 KLP59C inhibition perturbs chromosome segregation but not spindle assembly. **a**, Sequential images showing mitosis (metaphase and telophase) in an anti-KLP59C antibody-injected embryo containing rhodamine–tubulin (red) and GFP–histones (green). **b**, Sequential images illustrating improper kinetochore alignment (metaphase) and failed chromosome segregation (telophase) observed in an embryo containing rhodamine–histones (red) and GFP–Cid-labelled kinetochores (green). Although chromosomes do not segregate into daughter nuclei, sister kinetochores have segregated into two distinct sets at opposite sides of the chromosome mass. The arrow indicates a cluster of kinetochores that have failed to align properly. **c**, Plots of spindle length over time in control (red circles) and anti-KLP59C antibody-injected (black circles) embryos (beginning at prometaphase). **d**, Graph showing the average centroid positions of kinetochores on spindles from control (green triangles) and anti-KLP59C antibody-injected (red circles) embryos. Red stars mark the average position of spindle poles in spindles from KLP10A-inhibited embryos and green stars mark the average position of poles from controls.

injected NT proteins (Supplementary Fig. S10). Thus, our antibodies have the capacity to specifically precipitate endogenous KLP10A or KLP59C from their sites of action. Finally, it does not appear that the defects observed after KinI inhibition are due to an inhibition of the assembly of other functionally important proteins onto centromeres, kinetochores or centrosomes (where KLP10A and/or KLP59C localize). Indeed, KinI antibody injections do not overtly perturb the localization of a variety of GFP-tagged proteins that normally target to these spindle structures (Figs 2d, 3b, d and 4c; see also Supplementary Fig. S11). Instead, it is most likely that our antibodies specifically prevent targeting of the KinI proteins.

Together, these analyses reveal that both KLP10A and KLP59C perform functions needed to move chromatids poleward during anaphase. Furthermore, KLP10A performs an additional function involved in organizing spindle microtubules.

The capacity of KinI kinesins to depolymerize microtubules *in vitro*[10] (Supplementary Fig. S3), along with our observations that both KLP10A and KLP59C function in chromosome segregation, is consistent with the hypothesis that anaphase chromatid-to-pole motion requires the KinI-induced depolymerization of kinetochore microtubule ends. To test this hypothesis further, we examined the behaviour of spindle microtubules in the presence and absence of specific KLP10A and KLP59C inhibitors. Spindle microtubule dynamics were tracked using fluorescent speckle microscopy (FSM)—a technique in which dilute levels of rhodamine-labelled tubulin are microinjected into cells, resulting in the random incorporation of fluorescent tubulin 'speckles' into the microtubule lattice[17]. Speckles serve as markers that allow the direct observation of the dynamic behaviours of individual spindle microtubules. In controls, FSM reveals the persistent poleward movement of tubulin subunits within microtubule polymer lattices; that is, poleward flux (Fig. 4a; see also Supplementary Movie 6), as previously characterized[18,19].

The simultaneous imaging of GFP-tagged kinetochores and tubulin speckles provides an *in vivo* method to distinguish between the depolymerization of kinetochore microtubule plus or minus ends; flux requires kinetochore microtubule minus-end depolymerization at spindle poles, and kinetochores that move poleward more rapidly than speckles must depolymerize kinetochore microtubules at their plus ends. Consistent with previous reports, we find that the average rate of poleward flux is identical during metaphase and anaphase A ($0.037\,\mu m\,s^{-1}$) and is consistently slower than chromatid-to-pole movement (average rate: $0.094\,\mu m\,s^{-1}$, Fig. 4c; see also Supplementary Table S4)[18,19]. This suggests that poleward flux can contribute approximately 40% to the rate of anaphase chromatid-to-pole motion whereas Pac-Man-based motility can contribute roughly 60%. Moreover, these data directly demonstrate that kinetochore microtubules simultaneously depolymerize at both plus and minus ends during anaphase in *Drosophila* embryos.

To test the role of KLP10A in spindle microtubule depolymerization, FSM was performed in embryos injected with anti-KLP10A antibodies (Fig. 4a). In contrast to control embryos, fluorescent

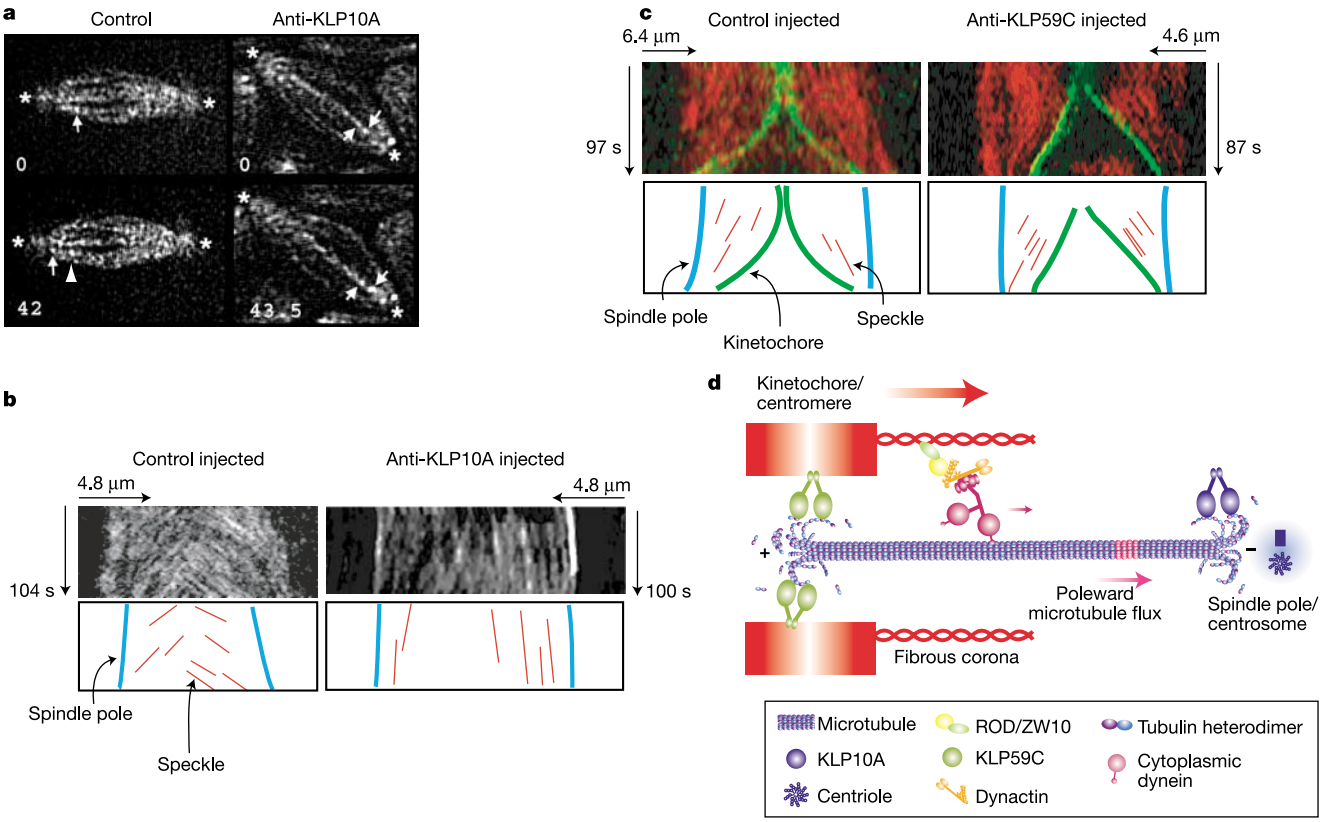

Figure 4 KLP10A is required for poleward flux whereas KLP59C is required for Pac-Man-based chromosome motility. **a**, Sequential FSM images of tubulin-speckle-labelled spindles from control and anti-KLP10A antibody-injected embryos. Time (in seconds) and centrosome positions (asterisk) are indicated. In the left panel, the arrow follows a speckle as it 'fluxes' poleward. The arrowhead (bottom) marks the approximate starting position of the speckle. In the right panel, the arrows track the position of two speckles over the same time period. These show little poleward displacement. **b**, Kymographs (top) and tracings (bottom) of fluorescent tubulin-labelled speckle movement on prometaphase/metaphase spindles from both conditions. **c**, Kymographs and tracings showing the movement of kinetochores (green) and tubulin-labelled speckles (red) on spindles from control and anti-KLP59C antibody-injected embryos. **d**, Model[9,30].

tubulin speckles either do not move poleward at detectable velocities or move at velocities that are significantly slowed (Supplementary Movie 7). Kymograph analysis of speckle movements confirms the point tracking of speckles and spindle edges (Fig. 4b; see also Supplementary Table S4). Indeed, >90% of speckles in KLP10A-inhibited spindles either do not have measurable motion or move at a reduced rate (Supplementary Fig. S12). Thus, KLP10A is required for normal poleward flux, making it the first molecular component of this phenomenon identified so far. On the basis of the proximity of this protein to microtubule minus ends at poles, our findings suggest that KLP10A promotes flux by actively depolymerizing kinetochore microtubules at their minus ends.

These data, along with the phenotypes observed after KLP10A inhibition described above, are notable in that they suggest roles for poleward flux in both anaphase chromatid-to-pole motion and in constraining the length of the mitotic spindle through metaphase[20] (see above). Although our focus here is on the former finding, the latter is also intriguing given the recent report that poleward flux ceases during anaphase B[18] (which occurs after chromatids have moved completely poleward). Thus, inactivation of spindle-pole-associated KinI proteins may normally serve as a trigger for anaphase spindle elongation.

In contrast to our KLP10A findings, KLP59C inhibition does not reduce the velocity of poleward tubulin speckle movement within spindles (Supplementary Table S4). However, kymographs comparing kinetochore movements to poleward flux reveal that, after KLP59C inhibition, kinetochores move poleward at the rate of flux but no faster, a decrease from control rates by roughly 60% (Fig. 4c; see also Supplementary Table S4). Indeed, under these conditions, kinetochores rarely bypass speckles on poleward-moving spindle microtubules, a phenomenon regularly observed in controls. Thus, KLP59C inhibition causes kinetochores to lose the ability to move along kinetochore microtubules and leaves them to behave solely as kinetochore microtubule anchors. Given the KLP59C localization to centromeres and its ability to destabilize microtubules *in vitro*, we conclude that this protein actively depolymerizes kinetochore microtubule plus ends and thus, it is the first required molecular component of Pac-Man-based chromatid motility identified so far.

Taken together, our findings support the mechanism for anaphase chromatid-to-pole movement shown in Fig. 4d. In this model, poleward driving forces acting on chromosomes result from the simultaneous disassembly of kinetochore microtubules at both minus and plus ends. At the minus ends, KinI-induced disassembly allows chromosome-associated kinetochore microtubules to be driven back into the poles (poleward flux). This activity probably requires additional factors that slide microtubules poleward. At the other end of kinetochore microtubules, centromere-associated KinI proteins act to disassemble kinetochore microtubule plus ends, causing them to shorten (Pac-Man). We propose that the minus-end-directed motor, cytoplasmic dynein, participates in this process by feeding kinetochore microtubules into the kinetochore[21]. It is tempting to speculate that this coupled, KinI-dependent, 'Pac-Man flux' model is conserved among phyla that contain KinI kinesins[9,11–13,22–25], although further work is required to establish this. If so, KinI motors will be promising targets for anti-tumour therapy. Although there are probably additional complexities to anaphase chromosome motility, the concerted action of flux and Pac-Man-based motility mechanisms provides the cell with a surprisingly dynamic means of segregating chromosomes. □

Methods

Drosophila KinI sequence data are described in Supplementary Fig. S2 legend.

Double-stranded RNAi

S2 cell culture and RNAi was performed as described[26]. Molecular methods are described in Supplementary Fig. S4 legend.

Immunofluorescence microscopy

For immunostaining, S2 cells were fixed exactly as described[26]. Antibodies were diluted to concentrations ranging from 1 to 20 $\mu g\ ml^{-1}$ (DM1a (Sigma), 1:200; GTU-88 (Sigma), 1:500; chicken anti-Cid (from G. Karpen), 1:500; rabbit anti-KLP10A 654, 655 and 656, 1:100; rabbit anti-KLP59C 696 and 698, 1:100). Secondary antibodies (Cy2-conjugated, rhodamine red X-conjugated and Cy5-conjugated anti-rabbit, mouse or chicken (Jackson ImmunoResearch)) were used at final dilutions of 1:100. Cells were mounted in Prolong (Molecular Probes). Propidium iodide (Sigma) was used at a concentration of 0.2 $mg\ ml^{-1}$. Mitotic S2 chromosomes were purified as described[27]. Specimens were imaged using a spinning-disk confocal microscope and displayed as maximum intensity projections.

Antibodies

DNA constructs are described in Supplementary Fig. S2 legend. *Escherichia coli*-expressed proteins were purified on either glutathione–Sepharose or amylose resin. Anti-glutathione S transferase (GST)–10A-NT, anti-GST–59C-NT and anti-GST–59D-NT antiserum was produced in rabbits (Covance). Antibodies were affinity-purified against their respective MBP fusion proteins precoupled to Affigel 10/15 (Bio-Rad) and eluted with low-pH buffer.

Microtubule depolymerization assays

Visual and sedimentation analyses of stabilized microtubule depolymerization were performed as previously described[10] with purified baculovirus-expressed $(His)_6$-tagged XKCM1 (50 nM), or with the purified, bacterially expressed $(His)_6$-tagged catalytic domain (500 nM) of either KLP10A (amino acids 204–609) or KLP59C (amino acids 158–568).

Drosophila stocks and embryo collection

The following transgenic flies were provided: GFP–histone from R. Saint and W. Sullivan; GFP–tubulin from A. Spradling; GFP–Cid from S. Henikoff; GFP–MeiS332 from T. Orr-Weaver; GFP–Rod from R. Karess; GFP–Polo from C. Sunkel and GFP–DTACC from J. Raff. Fly stocks were maintained and embryos collected as described[28].

Embryo microinjection

Microinjections were performed as described[28]. Rhodamine-labelled tubulin was purchased from Cytoskeleton. Rhodamine-labelled histones were prepared as described[29]. Control embryos were injected with nonspecific rabbit IgG, GST or buffer. GST, GST-tagged 10A-NT and GST-tagged 59C-NT proteins (see Supplementary Fig. S2c) were purified in PBS and microinjected at a range of concentrations (GST at 15–30 μM and GST–10A-NT, GST–59C-NT and GST–59D-NT at 6–12 μM; final intracellular concentrations). Rhodamine labelling of GST–KinI NT proteins was performed on glutathione–Sepharose-bound material according to a modified protocol[29], and injected at low concentration (GST–10A-NT at 1.8 μM, GST–59C-NT at 1.4 μM; final intracellular concentrations). Affinity-purified anti-KinI antibodies (see Supplementary Fig. S4) were microinjected at a range of concentrations (anti-KLP10A at 0.16–0.19 $mg\ ml^{-1}$, anti-KLP59C at 0.22–0.28 $mg\ ml^{-1}$; final intracellular concentrations). Anti-KLP10A Fabs (from affinity-purified 656 IgG) and anti-KLP59C Fabs (from affinity-purified 696 IgG) were prepared using ImmunoPure Fab Kit (Pierce) and injected at a final concentration of 0.05 and 0.08 $mg\ ml^{-1}$, respectively. Cy5 labelling of affinity-purified antibodies was performed using the Zenon Alexa Fluor-647 Labeling Kit (Molecular Probes).

Spinning disk confocal microscopy and FSM

Images and time-lapse movies were acquired using an UltraView Spinning Disk Confocal (PerkinElmer) mounted on a Nikon Eclipse TE 300 inverted microscope with a ×60, 1.4 N.A. objective. Multiple 1-μm *z*-sections were obtained using a piezo-electric *z*-axis controller for four-dimensional data set collection. FSM in embryos was performed as previously described[18]. Briefly, embryos were injected with dilute concentrations of rhodamine–tubulin (final intracellular concentration of 1–5 $\mu g\ ml^{-1}$) and sections of a single *z*-plane were acquired over time.

Image processing and data analysis

Data sets were saved as stacks of TIFF files. Z-series were saved as maximum intensity projections and time series were saved as AVI movies. Data sets were processed and analysed with MetaMorph (Universal Imaging). Analyses of mitotic phenotypes were restricted to a region approximately one-third of the embryo originating from the site of injection (see Supplementary Fig. S7). Where noted, statistical analysis was performed using a two-tailed, two-sample *t*-test for independent samples after first testing variance equality using an *F* test. FSM images were processed as follows: background was subtracted, regions of interest were passed through a Sharpen high filter, then a 4 × 4 low-pass filter, and finally, pixel intensities were 'multiplied' 9/6. Point-tracking motion analysis was performed by 'hand' using the Calipers tool. Motion analyses were also performed using the kymograph function. Kinetochore alignment was assessed as follows: the centroid position of all kinetochores on a spindle was averaged and plotted in relation to the centroid of the entire spindle. Note that all data points in these analyses represent the averaged position of all kinetochores on a spindle.

Received 17 September; accepted 28 November 2003; doi:10.1038/nature02256.
Published online 14 December 2003.

1. Mitchison, T. J. & Salmon, E. D. Mitosis: a history of division. *Nature Cell Biol.* **3,** E17–E21 (2001).
2. Wittmann, T., Hyman, A. & Desai, A. The spindle: a dynamic assembly of microtubules and motors. *Nature Cell Biol.* **3,** E28–E34 (2001).
3. Rieder, C. L. & Salmon, E. D. The vertebrate cell kinetochore and its roles during mitosis. *Trends Cell*

Biol. **8,** 310–318 (1998).
4. Mitchison, T. J., Evans, L., Schulze, E. & Kirschner, M. Sites of microtubule assembly and disassembly in the mitotic spindle. *Cell* **45,** 515–527 (1986).
5. Gorbsky, G. J., Sammak, P. J. & Borisy, G. G. Chromosomes move poleward in anaphase along stationary microtubules that coordinately disassemble from their kinetochore ends. *J. Cell Biol.* **104,** 9–18 (1987).
6. Mitchison, T. J. Polewards microtubule flux in the mitotic spindle: evidence from photoactivation of fluorescence. *J. Cell Biol.* **109,** 637–652 (1989).
7. Hunter, A. W. & Wordeman, L. How motor proteins influence microtubule polymerization dynamics. *J. Cell Sci.* **24,** 4379–4389 (2000).
8. Wordeman, L. & Mitchison, T. J. Identification and partial characterization of mitotic centromere-associated kinesin, a kinesin-related protein that associates with centromeres during mitosis. *J. Cell Biol.* **128,** 95–104 (1995).
9. Walczak, C. E., Mitchison, T. J. & Desai, A. XKCM1: a *Xenopus* kinesin-related protein that regulates microtubule dynamics during mitotic spindle assembly. *Cell* **84,** 37–47 (1996).
10. Desai, A., Verma, S., Mitchison, T. J. & Walczak, C. E. KinI kinesins are microtubule-destabilizing enzymes. *Cell* **96,** 69–78 (1999).
11. Maney, T., Hunter, A. W., Wagenbach, M. & Wordeman, L. Mitotic centromere-associated kinesin is important for anaphase chromosome segregation. *J. Cell Biol.* **142,** 787–801 (1998).
12. Kline-Smith, S. L. & Walczak, C. E. The microtubule-destabilizing kinesin XKCM1 regulates microtubule dynamic instability in cells. *Mol. Biol. Cell* **13,** 2718–2731 (2002).
13. Walczak, C. E., Gan, E. C., Desai, A., Mitchison, T. J. & Kline-Smith, S. L. The microtubule-destabilizing kinesin XKCM1 is required for chromosome positioning during spindle assembly. *Curr. Biol.* **12,** 1885–1889 (2002).
14. Goldstein, L. S. B. & Gunawardena, S. Flying through the *Drosophila* cytoskeletal genome. *J. Cell Biol.* **150,** F63–F68 (2000).
15. Sullivan, W. & Theurkauf, W. E. The cytoskeleton and morphogenesis of the early *Drosophila* embryo. *Curr. Opin. Cell Biol.* **7,** 18–22 (1995).
16. Sullivan, W., Fogarty, P. & Theurkauf, W. E. Mutations affecting the cytoskeletal organization of syncytial *Drosophila* embryos. *Development* **118,** 1245–1254 (1993).
17. Waterman-Storer, C. M., Desai, A., Bulinski, J. C. & Salmon, E. D. Fluorescent speckle microscopy, a method to visualize the dynamics of protein assemblies in living cells. *Curr. Biol.* **8,** 1227–1230 (1998).
18. Brust-Mascher, I. & Scholey, J. M. Microtubule flux and sliding in mitotic spindles of *Drosophila* embryos. *Mol. Biol. Cell* **13,** 3967–3975 (2002).
19. Maddox, P., Desai, A., Oegema, K., Mitchison, T. J. & Salmon, E. D. Poleward microtubule flux is a major component of spindle dynamics and anaphase A in mitotic *Drosophila* embryos. *Curr. Biol.* **12,** 1670–1674 (2002).
20. Waters, J. C., Mitchison, T. J., Rieder, C. L. & Salmon, E. D. The kinetochore microtubule minus-end disassembly associated with poleward flux produces a force that can do work. *Mol. Biol. Cell* **7,** 1547–1558 (1996).
21. Sharp, D. J., Rogers, G. C. & Scholey, J. M. Cytoplasmic dynein is required for poleward chromosome movement during mitosis in *Drosophila* embryos. *Nature Cell Biol.* **2,** 922–930 (2000).
22. Troxell, C. L. *et al. pkl1*$^+$ and *klp2*$^+$: Two kinesins of the Kar3 subfamily in fission yeast perform different functions in both mitosis and meiosis. *Mol. Biol. Cell* **12,** 3476–3488 (2001).
23. West, R. R., Malmstrom, T., Troxell, C. L. & McIntosh, J. R. Two related kinesins, *klp5*$^+$ and *klp6*$^+$, foster microtubule disassembly and are required for meiosis in fission yeast. *Mol. Biol. Cell* **12,** 3919–3932 (2001).
24. West, R. R., Malmstrom, T. & McIntosh, J. R. Kinesins *klp5*$^+$ and *klp6*$^+$ are required for normal chromosome movement in mitosis. *J. Cell Sci.* **115,** 931–940 (2002).
25. Garcia, M. A., Koonrugsa, N. & Toda, T. Two kinesin-like KinI family proteins in fission yeast regulate the establishment of metaphase and the onset of anaphase. *Curr. Biol.* **12,** 610–621 (2002).
26. Rogers, S. L., Rogers, G. C., Sharp, D. J. & Vale, R. D. *Drosophila* EB1 is important for proper assembly, dynamics, and positioning of the mitotic spindle. *J. Cell Biol.* **158,** 873–884 (2002).
27. Bousbaa, H., Correia, L., Gorbsky, G. J. & Sunkel, C. E. Mitotic phosphoepitopes are expressed in Kc cells, neuroblasts and isolated chromosomes of *Drosophila melanogaster. J. Cell Sci.* **110,** 1979–1988 (1997).
28. Sharp, D. J., Yu, K. R., Sisson, J. C., Sullivan, W. & Scholey, J. M. Antagonistic microtubule-sliding motors position mitotic centrosomes in *Drosophila* early embryos. *Nature Cell Biol.* **1,** 51–54 (1999).
29. Valdes-Perez, R. E. & Minden, J. S. *Drosophila melanogaster* syncytial nuclear divisions are patterned: time-lapse images, hypothesis and computational evidence. *J. Theor. Biol.* **175,** 525–532 (1995).
30. McIntosh, J. R., Grishchuk, E. L. & West, R. R. Chromosome-microtubule interactions during mitosis. *Annu. Rev. Cell Dev. Biol.* **18,** 193–219 (2002).

Supplementary Information accompanies the paper on **www.nature.com/nature**.

Acknowledgements We would like to thank B. Kenigsberg, D. Buster, P. Baas, F. McNally, A. Asenjo and H. Sosa for critically reading the manuscript; I. Brust-Mascher for advice on FSM; and A. Desai and J. Minden for help with rhodamine-histone preparations. We also thank C. Sunkel for providing GFP-Polo kinase flies and protocols for isolating mitotic chromosomes. We are grateful to the following individuals for their gifts: GFP–tubulin flies from A. Spradling; GFP-DTACC flies from J. Raff; GFP–Rod flies from R. Karess; GFP-Cid flies from S. Henikoff; and G. Karpen for the anti-Cid antibody. We thank G. Law, P. Franklin and R. Sleeper (PerkinElmer) for their assistance with the Ultraview confocal microscope. This work was supported by grants from the National Institutes of Health to D.J.S., C.E.W, R.D.V. and J.M.S.. C.E.W is a Scholar of the Leukemia and Lymphoma Society.

Competing interests statement The authors declare that they have no competing financial interests.

Correspondence and requests for materials should be addressed to D.J.S. (dsharp@aecom.yu.edu).

The MAPK Hog1 recruits Rpd3 histone deacetylase to activate osmoresponsive genes

Eulàlia de Nadal[1], Meritxell Zapater[1], Paula M. Alepuz[1]*, Lauro Sumoy[2], Glòria Mas[1] & Francesc Posas[1]

[1]*Cell Signaling Unit, Departament de Ciències Experimentals i de la Salut, Universitat Pompeu Fabra (UPF), and* [2]*Centre de Regulació Genòmica (CRG), E-08003 Barcelona, Spain*

* Present address: Departamento de Bioquímica y Biología Molecular, Universidad de Valencia, E-46100 Valencia, Spain

Regulation of gene expression by mitogen-activated protein kinases (MAPKs) is essential for proper cell adaptation to extracellular stimuli. Exposure of yeast cells to high osmolarity results in rapid activation of the MAPK Hog1, which coordinates the transcriptional programme required for cell survival on osmostress[1]. The mechanisms by which Hog1 and MAPKs in general regulate gene expression are not completely understood, although Hog1 can modify some transcription factors[2]. Here we propose that Hog1 induces gene expression by a mechanism that involves recruiting a specific histone deacetylase complex to the promoters of genes regulated by osmostress. Cells lacking the Rpd3–Sin3 histone deacetylase complex are sensitive to high osmolarity and show compromised expression of osmostress genes. Hog1 interacts physically with Rpd3 *in vivo* and *in vitro* and, on stress, targets the deacetylase to specific osmostress-responsive genes. Binding of the Rpd3–Sin3 complex to specific promoters leads to histone deacetylation, entry of RNA polymerase II and induction of gene expression. Together, our data indicate that targeting of the Rpd3 histone deacetylase to osmoresponsive promoters by the MAPK Hog1 is required to induce gene expression on stress.

In response to high osmolarity, Hog1 coordinates the transcription programme required for cell adaptation, and thus *hog1Δ* cells are osmosensitive[3]. Hog1 tightly binds chromatin in response to osmostress and elicits gene transcription by mechanisms other than the simple modification of activators[4,5]. To test whether the Hog1 MAPK can affect chromatin organization, we screened for osmosensitive mutants on the basis that mutations in chromatin-modifying activities that affect osmostress gene expression should result in cells that are osmosensitive.

Deleting genes encoding the Rpd3 histone deacetylase and its interacting protein Sin3 rendered cells osmosensitive (Fig. 1a). Notably, strains containing the double mutation *hog1Δ rpd3Δ* or *hog1Δ sin3Δ* were as osmosensitive as the single *hog1Δ* strain (data not shown). Rpd3 is a member of a family of five related histone deacetylases in yeast that also comprises Hda1, Hos1, Hos2 and Hos3. Deleting the genes encoding these related deacetylases did not affect cellular osmosensitivity (Fig. 1a and data not shown).

As histone deacetylases are involved in regulating gene expression, we tested whether the expression of Hog1-dependent genes was affected by deleting *RPD3*. Time course experiments showed that the expression of various osmostress-inducible genes, such as *HSP12*, *STL1*, *CTT1*, *ALD3*, *ARO9*, *ENA1* and *GRE2*, was reduced in the *rpd3Δ* strain on stress (Fig. 1b and not shown). Thus, Hog1-mediated gene expression is impaired by deleting *RPD3*.

To assess the relevance of Rpd3 in Hog1-mediated gene expression, we used microarray analysis to compare gene induction in wild type and *rpd3Δ* strains on osmostress. A high proportion of the genes induced on stress was affected by deleting the deacetylase. Of the 222 genes induced more than twofold in response to stress, more than 90% showed a significant reduction in expression after a